Controlled Soft-Template Synthesis of Ultrathin C@FeS Nanosheets with High-Li-Storage Performance

Chen Xu,[†,‡,§] Yi Zeng,[†,‡] Xianhong Rui,[†] Ni Xiao,[†] Jixin Zhu,[†,‡] Wenyu Zhang,[†,‡,§] Jing Chen, Weiling Liu,[†] Huiteng Tan,[†,‡,§] Huey Hoon Hng,[†] and Qingyu Yan[†,‡,§,*]

[†]School of Materials Science and Engineering, Nanyang Technological University, Singapore 639798, Singapore, [‡]TUM CREATE Research Centre@NTU, Nanyang Technological University, Singapore 637459, Singapore, and [§]Energy Research Institute@NTU, Nanyang Technological University, Singapore 637553, Singapore

Metal sulfides have wide potential applications in energy conversion,[1,2] energy storage,[2−4] electronics,[5] and luminescence devices.[6−8] Inspired by exciting findings of new dimension-dependent properties of graphene,[9−14] ultrathin two-dimensional (2D) graphene-like nanosheets of metal sulfides are attracting greater research interest. For energy storage applications, such as electrode materials in lithium ion batteries (LIBs), 2D nanostructures of metal sulfides are desired to (1) enhance the effective interaction between the active materials and electrolyte; (2) shorten the diffusion length of the charge carriers.

2D nanostructures of some layered-structured metal sulfides, such as ZrS_2,[15] MoS_2,[4,16] and WS_2,[17] have been actively studied as electrode materials in LIBs due to their structural advantages in reversible Li storage processes. 2D nanosheets of those layered-structured metal sulfides can be obtained by exfoliation due to the weak Van Der Waals interaction between S−S layers. However, the metal elements in these sulfides, for example, Zr, Mo, and W are relatively heavy, which may limit their theoretical specific energies densities. For example, the theoretical capacities of MoS_2 and WS_2 are calculated to be 167.5 and 108 mAh g^{-1}, respectively, based on complete Li insertion with the formation of $LiMoS_2$ and $LiWS_2$. These values are much lower than the theoretical capacity of commercially used graphite electrode (i.e., 372 mAh g^{-1}). Direct growth of 2D ultrathin nanostructures of metal sulfides with nonlayered crystal structures is relatively less reported although some of them possess high energy/charge storage capacities. Some pioneer works, such as growth of single crystalline PbS (cubic lattice symmetry) nanosheets through 2D oriented attachments,[18] polycrystalline CdTe nanosheets formed through dipole−dipole

ABSTRACT
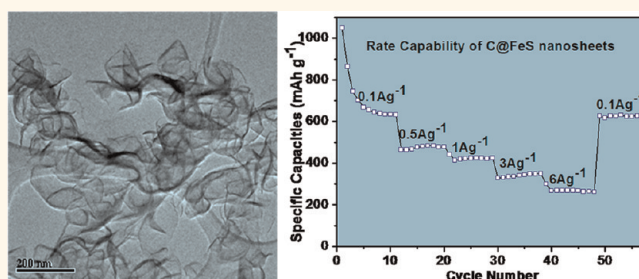
We report a facile approach to prepare carbon-coated troilite FeS (C@FeS) nanosheets *via* surfactant-assisted solution-based synthesis. 1-Dodecanethiol is used as both the sulfur source and the surfactant, which may form different-shaped micelles to direct the growth of nanostructures. Under appropriate growth conditions, the iron and sulfur atoms react to form thin layers of FeS while the hydrocarbon tails of 1-dodecanethiol separate the thin FeS layers, which turn to carbon after annealing in Ar. Such an approach can be extended to grow C@FeS nanospheres and nanoplates by modifying the synthesis parameters. The C@FeS nanosheets display excellent Li storage properties with high specific capacities and stable charge/discharge cyclability, especially at fast charge/discharge rates.

KEYWORDS: soft-template · 2D nanostructures · metal sulfides · iron · lithium ion battery

interactions,[19] and SnSe nanosheets with tuned thickness,[20] indicates the possibility of obtaining nanosheets of nonlayered metal sulfides *via* controlled self-assembling with effective capping ligands.

Iron sulfides are interesting materials for energy storage applications due to their cost effectiveness and abundance in nature. They have been tested as electrode materials in lithium primary batteries[21] and secondary batteries,[22] and they store Li *via* a conversion reaction. However, the Li storage process in the conversion-reaction-based metal sulfides involves generation of polysulfides Li_2S_x (2 < x < 8),[23,24] which can easily dissolve into an organic electrolyte
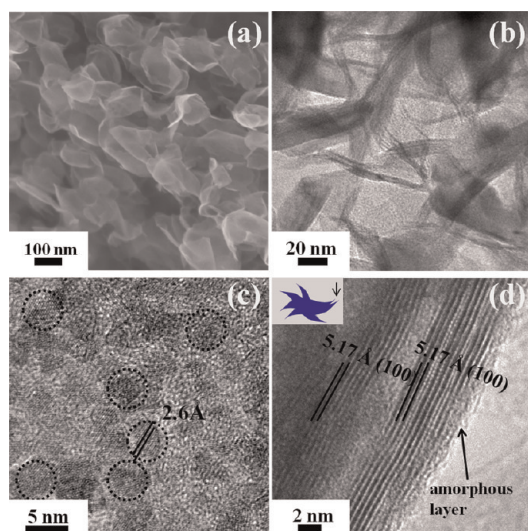
Figure 1. (a) SEM and (b) TEM images of as-prepared nanosheets; (c) top-view and (d) side-view HRTEM images of the polycrystalline nanosheets.
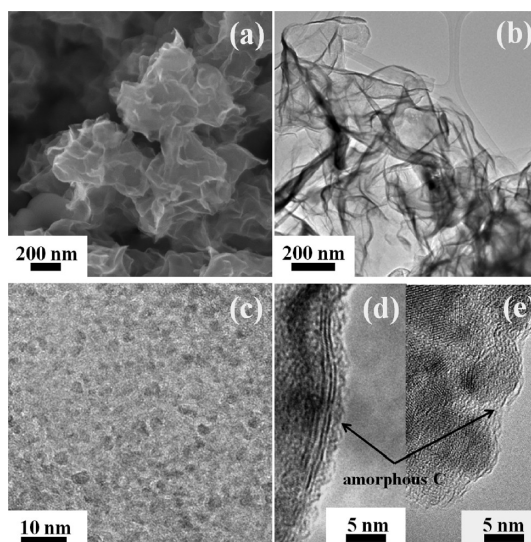

Figure 2. (a) SEM and (b) TEM images of the FeS nanosheets after annealing at 400 °C for 2 h under argon atmosphere; (c) top-view high-magnification TEM image of the annealed polycrystalline nanosheet; (d) side-view and (e) top-view HRTEM images of the annealed FeS nanosheet.

and migrate to the cathode side. This results in poor cyclability of LIBs. Recently, studies in Li–S battery showed that capping the sulfur into thin wrapping layers could effectively reduce the dissolution of Li_2S_x into the electrolyte, which led to high reversible capacities and good rate capabilities.[25−27] This could be a promising strategy for performance improvement in LIBs with metal sulfide electrodes, where the sulfides could be wrapped with a thin layer of carbon to reduce polysulfides dissolution into the electrolyte.

Herein, we report a facile approach to prepare graphene-like FeS nanosheets *via* a surfactant-assisted solution-based synthesis. The as-prepared FeS nanosheets are polycrystalline, suggesting that the growth of nanosheets is not related to the crystal structures and this approach may be extendable to synthesis of other sulfides. In this approach, 1-dodecanethiol is used as both the sulfur source and the surfactant, and different-shaped micelles could be formed by varying its concentration. Under appropriate growth conditions, the iron and sulfur atoms react to form thin layers of FeS while the hydrocarbon tails of 1-dodecanethiol separate the thin FeS layers to organize into a lamellar structure. The hydrocarbons can be converted to amorphous carbon after annealing at 400 °C for 2 h under argon atmosphere. Such an approach is extendable to grow C@FeS nanospheres and nanoplates by modifying the synthesis parameters. The C@FeS nanosheets displayed excellent Li storage properties with stable charge/discharge cycling performances. In particular, due to their advantageous nanostructure, the C@FeS nanosheets showed high capacities with stable cyclability at fast charge/discharge rates, for example, a discharge capacity of 260 mAh g^{-1} at a current density of 6000 mA g^{-1} (10C) during the 100th cycle.

RESULTS AND DISCUSSION

Morphology Characterization. A representative sample was prepared by reacting Fe(acac)$_3$ and 1-dodecanethiol (DDT) with a molar ratio, $I_{Fe:thiol}$, of Fe(acac)$_3$:DDT = 1:20 in oleylamine (OLA) at 220 °C. The SEM image in Figure 1a and TEM image in Figure 1b reveal the formation of graphene-like nanosheets with lateral lengths of 100−200 nm. These nanosheets are interconnected forming porous networks. Thicknesses of the nanosheets are determined to be in the range of 4−10 nm by AFM measurement (Figure SI1, Supporting Information) and TEM observation (Figure SI2, Supporting Information). The XRD pattern (Figure SI3, Supporting Information) shows that the as-prepared nanosheets are troilite FeS (JCPDF no. 00-037-0477) with no other phases. The peaks at 2θ = 29.95°, 33.71°, 43.18°, and 53.17° correspond to the (110), (112), (114), and (300) planes of troilite FeS, respectively. There is no predominant peak in the XRD pattern, indicating that there is no preferred crystalline orientation in the nanosheets. A top-view HRTEM image (Figure 1c) reveals the polycrystalline nature of an individual nanosheet comprising nanocrystals of sizes <5 nm as highlighted by the dotted circles. The observed lattice spacing of 2.6 Å corresponds to (112) planes of troilite FeS. The polycrystalline nature of the as-prepared FeS nanosheets suggests that the ultrathin 2D shape is not directly related to the crystal structure of FeS, and the formation mechanism is different from that of single-crystalline ZrS$_2$, MoS$_2$, WS$_2$, and Fe$_7$S$_8$ 2D structures.[15,28−30] The growth of the polycrystalline nanosheets may be induced by the soft template formed from the surfactants added. The selected area electron diffraction (SAED) (Figure SI4, Supporting Information)

confirms its troilite phase (JCPDF no. 037-0477), which is consistent with the XRD pattern. The HRTEM image in Figure 1d shows the cross-section area of the FeS nanosheets. It reveals amorphous coatings on the surface of the nanosheets, which is the capping surfactant. To convert the amorphous coating on the FeS nanosheets to carbon, the samples were annealed at 400 °C for 2 h under Ar atmosphere. After the annealing process, the nanosheet morphology shows no obvious change (Figure 2a–b). The XRD pattern (Figure SI3, Supporting Information) shows diffraction peaks corresponding to the (110), (112), (114), and (300) planes of troilite FeS. The top-view TEM image (Figure 2c) of the nanosheets reveals that they remain polycrystalline. The HRTEM images (Figure 2d,e) indicate that the FeS sheets are still embedded in amorphous layers, which is expected to be carbon. To verify the nature of the amorphous layers coated on the annealed FeS nanosheets, EDX elemental mappings of the nanosheets were obtained (Figure SI5, Supporting Information). The elemental mapping clearly indicates that there is a uniform dispersion of the carbon element in the FeS nanosheets besides of Fe and S. The carbon component was further studied using Raman spectra (Figure SI6, Supporting Information). The Raman signatures of G band ($\sim$1580 cm^{-1}) and a D1 band ($\sim$1340 cm^{-1}) confirm the existence of carbon, which is poorly crystallized and is similar to carbon formed by carbonization of organic surfactants.[31,32] Thus, the annealed sample is concluded to be carbon-coated FeS (C@FeS) nanosheets. Thermal gravimetric analysis (TGA) profile (Figure SI7, Supporting Information) of C@FeS nanosheets shows 15.5% weight loss by heating in air up to 900 °C, implying that 7% of the mass is carbon. The specific surface area of the annealed C@FeS nanosheets is calculated to be 80.9 m^2 g^{-1} on the basis of the Brunauer–Emmett–Teller (BET) analysis of the nitrogen absorption/desorption isotherm (Figure SI8, Supporting Information).

To investigate the growth details of the samples, we carried out the synthesis of FeS under different conditions. Replacing DDT with S-OLA (prepared by dissolving sulfur powder in oleylamine) as the sulfur source and keeping other synthesis parameters similar resulted in the growth of irregularly shaped nanocrystals (Figure SI9, Supporting Information). Increasing the molar ratio of $I_{Fe:thiol}$ to 1:4 by decreasing the amount of 1-dodecanethiol in the solution resulted in the formation of spherical nanoparticles (Figure 3a). The diameter of the spherical particles ranges from 30 to 100 nm. The TEM image (Figure 3b) reveals that each particle is a cluster composed of 2–3 nm grains embedded in an amorphous matrix. The HRTEM image and SAED pattern (Figure 3c,d) confirm that the nanograins are troilite FeS (JCPDF no. 00-037-0477). After annealing the sample at 400 °C for 2 h under Ar atmosphere, the spherical particles exhibit no noticeable change of either the shape or the nanostructures as observed by SEM and
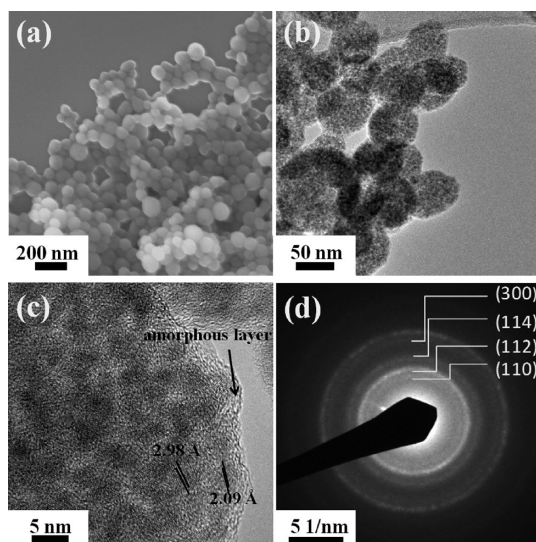

Figure 3. (a) SEM and (b) TEM images of the as-prepared FeS nanoparticles; (c) HRTEM image of the FeS nanoparticles showing nanograins embedded in an amorphous matrix; (d) selected area electron diffraction (SAED) pattern of the FeS nanoparticles.

TEM (Figure SI10a,b, Supporting Information). The nanograins remain embedded in the amorphous matrix. The Raman spectrum (Figure SI6, Supporting Information) of the spherical nanoparticles after annealing confirms that the amorphous matrix is amorphous carbon as indicated by the broad D (1340 cm^{-1}) and G (1580 cm^{-1}) bands.

Besides of the concentration of DDT, reaction temperature also plays an important role in determining the shapes of the FeS nanostructures. Increasing the reaction temperature from 220 to 280 °C and keeping $I_{Fe:thiol}$ = 1:20 (same as that for the growth of FeS nanosheets) leads to the formation of hexagonal-shaped nanoplates (Figure 4a,b). The XRD pattern of the nanoplates (Figure SI11, Supporting Information) reveals that they are also troilite FeS (JCPDF no. 00-037-0477) without any detectable crystalline impurity phase. These FeS nanoplates are uniform in shape with lateral diameters of 100–200 nm and thickness of around 50 nm. The HRTEM images of both top view and side view of a FeS nanoplate (Figure 4c,d) show that it is single crystalline with the normal of the primary surfaces along [001] direction. These FeS nanoplates are also coated with amorphous layers (Figure 4c,d), which convert to amorphous carbon after annealing under Ar atmosphere as indicated by the Raman spectrum of the annealed sample (Figure SI12, Supporting Information). Morphology of these nanoplates is retained after annealing (Figure SI10c,d, Supporting Information). The specific surface area of the annealed C@FeS nanoplates is calculated to be 28.87 m^2 g^{-1} on the basis of the BET analysis of the nitrogen absorption/desorption isotherm (Figure SI12, Supporting Information).

On the basis of the above observation, the proposed growth process of the C@FeS nanostructures
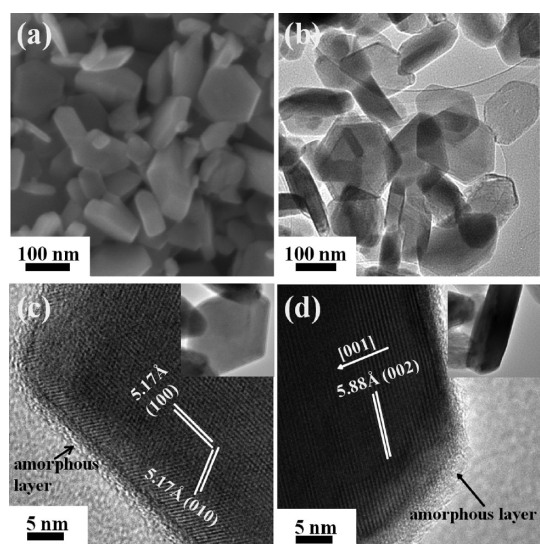
Figure 4. (a) SEM and (b) TEM images of as-prepared FeS nanoplates; (c) top-view and (d) side-view HRTEM images of the FeS nanoplates. Insets in panels c and d are the corresponding low-magnification TEM images showing the area where the HRTEM images were obtained.

(nanosheets, spherical nanoparticles, and nanoplates) are shown in Scheme 1. Here, several factors should be considered in the growth of the FeS nanostructures. Growth of single crystalline PbS nanosheets through oriented attachment of nanocrystals[18] has been previously reported. But, the FeS nanosheets obtained in this work are polycrystalline and those FeS nanocrystals show no preferred orientation and exposure of facets. Thus, the oriented attachments may be less involved here. Another possibility is the electrostatic interaction between the nanocrystals that lead to formation of thin sheets as previously reported for CdTe nanosheets.[19] In this reaction, the acidic DDT reacts with the basic OLA to form OLAH$^+$ and dodecane-thiolate anion,[33,34] the latter of which binds strongly to Fe and leads to formation of a dipole unit containing the Fe$-$S$^-$ headgroup and alkyl chain. The charged dipoles may induce the dipole$-$dipole interaction between nanocrystals and direct the nanosheet formation. Above all, the shape of micelles directed by DDT under different synthesis conditions is considered to be the key influential factor to the final morphology. Under a lower concentration of DDT ($I_{\text{Fe:thiol}}$ = 1:4), although the dipole units containing the Fe$-$S$^-$ still exists, polycrystalline spherical nanoparticles formed with the grain size similar to that aggregated as nanosheets formed at a higher concentration of DDT ($I_{\text{Fe:thiol}}$ = 1:20). If the dipole$-$dipole interaction[35] is the determining factor in the FeS nanosheets formation, we would expect to observe some FeS nanosheets at $I_{\text{Fe:thiol}}$ = 1:4 rather than the polycrystalline nanoparticles. Therefore, the shape of the micelles could be an important driving force for morphology variation. As illustrated in Scheme 1, we proposed that the Fe/DDT

complexes with lamellar structure act as the soft template for the nucleation and growth of polycrystalline FeS nanosheets, while the spherical micelles lead to the formation of polycrystalline FeS spherical particles. During the annealing process, the $-C_{12}$ tails may evolve to the amorphous layer to prevent the agglomeration of FeS nanocrystals across the lamellas or inside the spherical particles. However, at a higher temperature of 280 °C, the rapid diffusion process of the atoms may take place across the interfaces (*i.e.*, the amorphous layers and grain boundaries) to allow the formation of single-crystalline hexagonal FeS nanoplates. The shape of the single crystalline FeS nanoplates may be directly related to the crystal lattice structure of the troilite phase instead of the micellar shapes. A hexagonal symmetrical crystal lattice can lead to the growth of a plate-like shape mainly due to the confined growth within the (001) plane.[36,37] To examine the above discussion, low-angle XRD pattern of the room-temperature dried colloidal suspension was conducted for the solution reacting from $I_{\text{Fe:thiol}}$ = 1:20 in OLA (Figure SI13, Supporting Information). The XRD pattern shows a group of periodic reflection peaks at 2θ = 3.77°, 7.3°, 10.6°, 14.2°, 17.7°, 21.22°, and 24.68° with gradually decreased intensities suggesting the formation of the lamellar structure. The first-order reflection of the strong peak at 2θ = 3.77° corresponds to a *d*-spacing of 2.34 nm, and is larger than the 1-dodecanethiol molecular length (1.52 nm),[38] which implies a double layer of the hydrocarbon tails in between the Fe$-$S layers. The low intensities for the (002), (004), (006), and (008) peaks also prove the bilayer feature of the surfactants.[39] It should be noted that the small angle XRD measurement was performed at room temperature while the synthesis of the FeS nanostructures was carried out at temperatures >200 °C. The shape of the micelles could be affected by the temperature.[40] However, the above observation partially supports that there are lamellar soft templates formed in the precursor solution. DDT has been previously used only as sulfur sources for the synthesis of metal sulfides, for example, CdS nanowires,[41,42] flower-like Cu_2S, ZnS, and MnS nanocrystals,[43−45] but has not been demonstrated as a major controlling factor to morphologies of sulfide nanocrystals. More importantly, the amorphous layer on the FeS nanocrystals formed by the alkyl chains can be converted to carbon layers, which is important to achieve the desired anode performances of sulfides by reducing polysulfide dissolution into the electrolyte as discussed in the introduction.

Electrochemical Characterization. Comparative electrochemical characterization was conducted to investigate the anode performances of the C@FeS nanosheets, nanoplates, and nanoparticles based on two-electrode coin-type cells[46] with Li metal as the counter-electrode. All working electrodes for the following electrodes were fabricated from annealed powder samples. Figure 5a shows the cyclic voltagrams (CVs) of the C@FeS
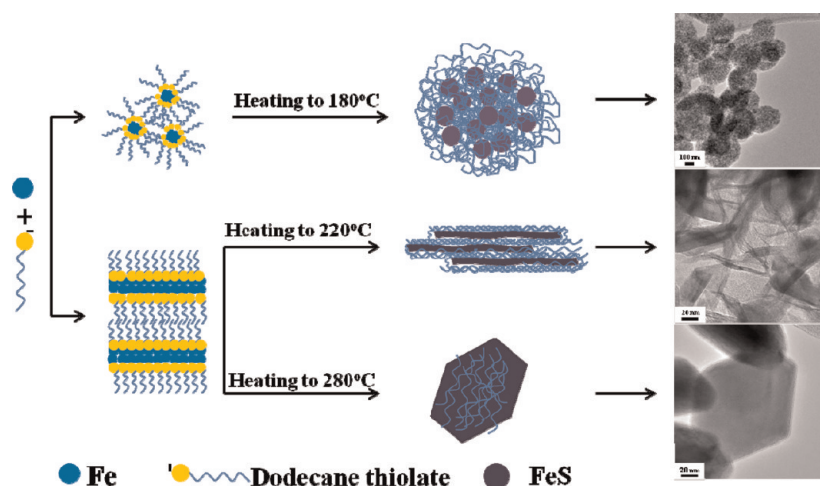
Scheme 1. Proposed reaction mechanism for the C@FeS nanoparticles, nanosheets, and nanoplates. FeS nanoparticles form at a low concentration of 1-dodecanethiol (e.g., $I_{Fe:thiol}$ = 1:4). 2D FeS nanostructures form at a high concentration of 1-dodecanethiol (e.g., $I_{Fe:thiol}$ = 1:20): (1) polycrystalline nanosheets form at a low T = 220 °C; and (2) single-crystalline nanoplates form at a high T = 280 °C. The amorphous layers formed by the alkyl chains can be converted to carbon layers after annealing.

nanosheets electrode at a scan rate of 0.5 mV/s between 0 and 3 V versus Li$^+$/Li for the first, second, and fifth discharge/charge cycles. In the first cycle discharge, a small peak at 1.65 V is observed, which corresponds to the reaction of Li with FeS forming Li$_2$FeS$_2$:[37] 2FeS + 2Li + 2e$^-$ = Li$_2$FeS$_2$ + Fe (1) A sharp peak at around 1.05 V is related to the conversion reaction:[22,24,47] FeS + 2Li + 2e$^-$ = Li$_2$S + Fe (2). The broad peak appearing from 0.75 to 0 V is attributed to the formation of a solid electrolyte interlayer,[47] which is missing in subsequent charge/discharge cycles. The peak at around 2.0 V in the first cycle corresponds to the oxidation of Fe to form Li$_{2-x}$FeS$_2$[28,30] as Fe + Li$_2$S $-$ xLi $-$ xe$^-$ $\rightarrow$ Li$_{2-x}$FeS$_2$ (3). Peaks at 1.3 V during the discharge of the second and fifth cycle are related to the formation of Li$_{2-x}$FeS$_2$[22,30] while peaks at around 2.0 V during the charge step are attributed to the delithiation process of Li$_2$FeS$_2$ to form Li$_{2-x}$FeS$_2$. Conversion between Li$_{2-x}$FeS$_2$ and Li$_2$FeS$_2$ is reversible, which enables the application of iron sulfides in rechargeable LIBs.

Charge/discharge voltage profiles of C@FeS nanosheets electrode at a current density of 0.1 A g^{-1} (0.16C) between 0.01 V and 3.0 V are shown in Figure 5b. The C@FeS nanosheets electrode delivers an initial discharge capacity of 1022 mAh g^{-1} and a subsequent charge capacity of 635 mAh g^{-1}, leading to a first-cycle Columbic efficiency of 62%. The large discharge capacity of C@FeS nanosheets electrode during the first cycle may be attributed to the formation of SEI layer and the irreversible reaction between Li and FeS as indicated in reactions 1 and 2. During the second cycle, the C@FeS nanosheets electrode delivers a discharge capacity of 668 mA g^{-1} and a charge capacity of 591 mAh g^{-1} with a much higher Columbic efficiency of 88.4%.

Good rate performance is crucial to achieving high power densities in LIBs. The rate performance of the C@FeS nanosheets electrode is plotted in Figure 5c. It

depicts ninth-cycle discharge capacities of around 630, 486, 425, and 349 mAh g^{-1} at current densities of 0.1 A g^{-1} (0.16C), 0.5 A g^{-1} (0.8C), 1 A g^{-1} (1.6C) and 3 A g^{-1} (5C), respectively. Even at a very high current density of 6 A g^{-1} (10C), the C@FeS nanosheets can still deliver a ninth-cycle discharge capacity of 266 mAh g^{-1}, which is higher than those reported for some of the state-of-art anodes at 10C, for example, 215 mAhg^{-1} for Fe$_2$O$_3$/graphene composite[48] and 150 mAh g^{-1} for ultrathin anatase TiO$_2$ nanosheets.[49] Moreover, the specific capacity of the C@FeS nanosheets electrode can recover to 630 mAh g^{-1} when the current density is reduced from 6 A g^{-1} (10C) to 0.1 A g^{-1}. The rate performance of C@FeS, both C@FeS nanoplates- and nanoparticles-based electrodes, was also investigated (Figure5c). The hierarchically structured C@FeS nanoparticles electrode shows ninth-cycle discharge capacities of 619 and 217 mAh g^{-1} at current densities of 0.1 A g^{-1} (0.16C) and 6 A g^{-1} (10C), respectively. The C@FeS nanoplates electrode displays lower ninth-cycle discharge capacities of 530 and 133 mAh g^{-1} at current densities of 0.1 A g^{-1} (0.16C) and 6 A g^{-1} (10C), respectively. The excellent rate performance of the C@FeS nanosheets is mainly due to their small grains and ultrathin thickness: (1) it provides a larger effective interaction area between electrode materials and electrolyte; (2) it shortens the Li diffusion path and improves the kinetics of charge carrier transport. The difference between the rate capability of the C@FeS nanosheet electrode and nanoplate electrode is verified by the electrochemical impedance spectra (EIS) on the samples after 5 discharge/charge cycles. The C@FeS nanosheets electrode exhibits a smaller radius of semicircle in the Nyquist plots (Figure SI15, Supporting Information), which inidcates a lower charge-transfer resistance than that of C@FeS nanoparticles and nanoplates electrode.
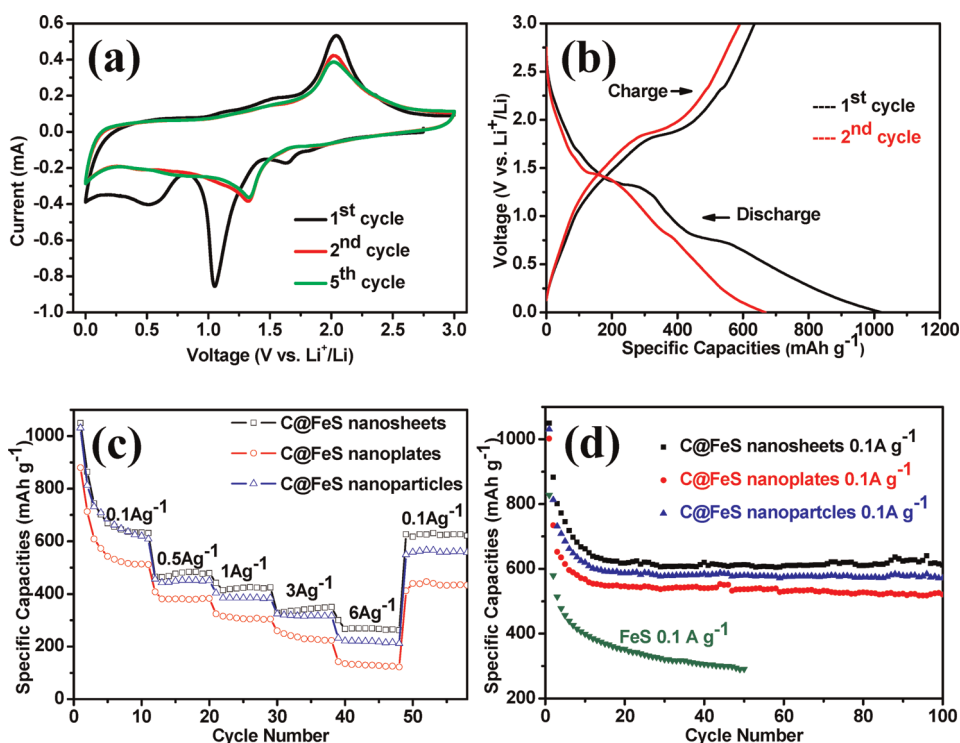
Figure 5. (a) Cyclic voltammetries of the C@FeS nanosheets electrode between 0 and 3 V at a scan rate of 0.5 mV s^{-1} for the 1st, 2nd, and 5th cycles; (b) charge−discharge voltage profiles of the C@FeS nanosheets electrode at a current density of 0.1 A g^{-1} for the 1st and 2nd cycles; (c) cycling performance of the C@FeS nanosheets electrode, C@FeS nanoplates electrode, and C@FeS nanoparticles electrode at various current densities; (d) comparison of the cycling performance of C@FeS nanosheets electrode, C@FeS nanoparticles electrode, C@FeS nanoplates electrode, and bare FeS nanocrystals electrode at 0.1 A g^{-1}.

Stable cyclic performance of electrode materials is important for practical application of LIBs. The discharge/charge cycling stability of annealed C@FeS nanosheet-, nanoparticle-, and nanoplate-based electrodes were examined at a current density of 0.1 A g^{-1} (0.16 C) between 0.01 and 3.0 V (Figure 5d). At a current density of 0.1 A g^{-1}, the discharge capacity of the C@FeS nanosheets electrode is 623 mAh g^{-1} during the 20th cycle and remains at 615 mAh g^{-1} during the 100th cycle, indicating a stable cyclability. The hierarchically structured C@FeS nanoparticles also exhibit good cyclability with discharge capacities of 592 mAh g^{-1} during the 20th cycle and 580 mAh g^{-1} during the 100th cycle. Although the C@FeS nanoplates electrode has a lower specific capacity, it still exhibits an acceptable cycling performance. It depicts a specific capacity of 550 mAh g^{-1} during the 20th cycle, which maintains at 525 mAh g^{-1} during the 100th cycle. We also measured the discharge/charge cycling stability of as-synthesized (before annealing) FeS nanosheet-, nanoparticle- and nanoplate-based electrodes at a current density of 0.1 A g^{-1} (0.16 C) between 0.01 V and 3.0 V (Supporting Information Figure SI14). These electrodes depict lower capacities as compared to those of annealed ones, for example, delivering 50th-cycle discharge capacities of 261 mAh g^{-1}(nanosheets), 281 mAh g^{-1}-(nanoparticles), and 225 mAh g^{-1}(nanoplates). There are capping layers on the surface of these as-synthesized

nanostructures, which affect effective charge transfer in these electrodes.

For comparison, we also prepared FeS nanoparticles by mixing 0.05 M Na$_2$S and 0.05 M FeCl$_2$ in DI water under vigorous stirring for 1 h in argon atmosphere. The SEM image (Figure SI16a, Supporting Information) shows nanocrystals of ∼30 nm, while the corresponding XRD pattern (Figure SI16b, Supporting Information) confirms that they are troilite FeS. The HRTEM image (Figure SI16c, Supporting Information) shows that there is no trace of amorphous carbon layer on these FeS nanoparticles after annealing, which is consistent with the Raman measurement (Figure SI16d, Supporting Information). The cycling performance of the bare FeS nanoparticles is also plotted in Figure 5d, indicating a poor cyclability. At a current density of 0.1 A g^{-1}, the specific capacity of the bare FeS nanoparticles is 404 mAh g^{-1} during the 10th cycle, which quickly decays to 292 mAh g^{-1} during the 50th cycle. Although bare FeS nanoparticles might be gradually oxidized in humid air (as indicated by XPS in Figure SI17 in Supporting Information), the presence of iron oxides should not be a major factor in the poor electrochemical performance, because both Fe$_3$O$_4$ and Fe$_2$O$_3$ are suitable Li storage materials.[50−52] The improved cycling stability of C@FeS nanostructures-based electrode than that of the bare FeS nanocrystals-based electrode may be attributed to the dissolution of

polysulfides for the bare FeS nanocrystals.[23,24] CHNS elemental analysis (Table S1 with detailed sample preparation, Supporting Information) shows that electrodes based on C@FeS nanosheets have less polysulfide dissolved in the electrolyte than that based on bare FeS nanocrystals, which further supports the carbon effect on preventing polysulfide dissolution and sustaining cycling stability.

CONCLUSION

In summary, carbon-coated FeS (C@FeS) nanosheets are prepared *via* a surfactant-assisted solution-based synthesis technique, in which 1-dodecanethiol is used as both the sulfur source and surfactant. With adjustable synthesis conditions, C@FeS nanoplates and nanoparticles can also be prepared. The C@FeS nanosheets deliver promising Li storage properties with high specific capacities, stable cyclabilities, and good rate performances. It depicts a specific capacity of 233 mAh g^{-1} during the 100th cycle at a 10-C discharge rate, which is attractive for the development of LIBs with high power densities and high energy densities. The excellent Li storage performance of the C@FeS nanosheets is mainly attributed to (1) the open networks of C@FeS nanosheets that can effectively accommodate large volume changes induced during the charge/discharge process; (2) the ultrathin thickness of the nanosheets shortens the diffusion paths of charge carriers and allows faster charge transfer; (3) the carbon layers can absorb and trap the polysulfides generated during the conversion reaction of sulfides, which reduces the dissolution of polysulfides, and improves the cycling stability of the electrode.

METHODS

Chemical Synthesis. The solvothermal synthesis was carried out in a three-neck flask. Typically, 0.2 mmol (70 mg) Fe(acac)$_3$ (Aldrich) was first dissolved to 10 mL in oleylamine (OLA)-(Aldrich, 70%) under magnetic stirring, and then argon gas was introduced to purge the solution. After about 30 min of purging, the solution was gradually heated up to 120 °C to completely dissolve Fe(acac)$_3$ to form a red-wine transparent solution. One milliliter of 1-dodecanethiol (Aldrich, 98%) was then injected into the solution at 120 °C, and the solution turned transparent light-yellow. The solution was then stirred at 120 °C for 30 min before the temperature was further increased to 220 °C, and the solution turned opaque black. The reaction mixture was maintained at 220 °C for 20 min before being allowed to naturally cool down to room temperature. The resultant solution was dripped into hexane, and the precipitates were collected by centrifugation. The final product was dried in a vacuum oven.

Morphology Characterization. Morphologies were characterized by a field emission scanning electron microscope (FESEM, JEOL JSM-7600F). The HRTEM images were observed using a transmission electron microscope (TEM, JEOL 2010) operating at 200 kV. Crystal phases were identified using X-ray diffractometer (Shimadzu) with Cu Kα irradiation. Raman spectra were obtained with a WITec CRM200 confocal Raman microscopy system with a laser wavelength of 488 nm and a spot size of 0.5 mm. To calibrate the wavenumber, the Si peak at 520 cm^{-1} was used as a reference. Nitrogen adsorption/desorption isotherms were measured on a Micromeritics Tristar 3000 porosimeter (mesoporous characterization) and Micromeritics ASAP 2020 (microporous characterization) at 77 K. Samples were degassed at 100 °C for 6 h under vacuum before measurement. The specific surface areas were calculated using Brunauer−Emmet−Teller (BET) method. The AFM images were obtained using a Dimension 3100 (Veeco, CA, USA) in a tapping mode with a Si tip under ambient conditions.

Electrochemical Characterization. The as-synthesized samples were annealed in a tube furnace at 400 °C for 2 h under argon atmosphere. Then, 80 wt % active materials, 10 wt % super-P carbon black and 10 wt % polyvinylidene fluorides (PVDF) were mixed into *N*-methyl-2-pyrrolidinone (NMP). The obtained slurry was cast onto a copper foil and dried in vacuum at 50 °C for 12 h to remove excess solvent. Electrochemical measurements were carried out on coin-type cells[48,53] with lithium metal as the counter/reference electrode, Celgard 2400 membrane as the separator, and the electrolyte solution obtained by dissolving 1 M LiPF$_6$ into a mixture of ethylene carbonate (EC) and dimethyl carbonate (DMC) (EC/DMC, 50: 50 w/w). The cells were tested on a NEWARE multichannel battery test system with galvanostatic charge and discharge (voltage window of 0.01−3.0 V). Cyclic voltammetry (0−3 V, scan rate of 0.5 mV s^{-1}) was carried out with an electrochemical workstation (Solartron). It should be noted that the specific capacity was calculated on the basis of the total mass of the C@FeS composites.

Conflict of Interest: The authors declare no competing financial interest.

Supporting Information Available: AFM image of nanosheets, XRD patterns for nanosheets and nanoplates, SEAD pattern of as-synthesized FeS nanosheets, TEM−EDX elemental mapping, SEM image of nanocrystals synthesized using S-OLA as the sulfur source, SEM and TEM images of C@FeS nanospheres and nanoplates after annealing, Raman spectrum, nitrogen adsorption/desorption isotherms, Nyquist plots, and information regarding bare FeS nanocrystals. This material is available free of charge *via* the Internet at http://pubs.acs.org.

REFERENCES AND NOTES

1. Xin, X.; He, M.; Han, W.; Jung, J.; Lin, Z. Low-Cost Copper Zinc Tin Sulfide Counter-electrodes for High-Efficiency Dye-Sensitized Solar Cells. *Angew. Chem., Int. Ed.* **2011**, *50*, 11739–11742.

2. Lai, C.-H.; Lu, M.-Y.; Chen, L.-J. Metal Sulfide Nanostructures: Synthesis, Properties and Applications in Energy Conversion and Storage. *J. Mater. Chem.* **2012**, *22*, 19–30.

3. Xiao, J.; Choi, D.; Cosimbescu, L.; Koech, P.; Liu, J.; Lemmon, J. P. Exfoliated MoS$_2$ Nanocomposite as an Anode Material for Lithium Ion Batteries. *Chem. Mater.* **2010**, *22*, 4522–4524.

4. Feng, C.; Ma, J.; Li, H.; Zeng, R.; Guo, Z.; Liu, H. Synthesis of Molybdenum Disulfide (MoS$_2$) for Lithium Ion Battery Applications. *Mater. Res. Bull.* **2009**, *44*, 1811–1815.

5. Wu, L.; Quan, B.; Liu, Y.; Song, R.; Tang, Z. One-Pot Synthesis of Liquid Hg/Solid β-HgS Metal−Semiconductor Heterostructures with Unique Electrical Properties. *ACS Nano* **2011**, *5*, 2224–2230.

6. Li, N.; Zhang, X.; Chen, S.; Yang, W.; Kang, H.; Tan, W. One-Pot Self-Assembly of Flower-like Cu$_2$S Structures with Near-Infrared Photoluminescent Properties. *CrystEngComm* **2011**, *13*, 6549–6554.

7. Deng, Z.; Tong, L.; Flores, M.; Lin, S.; Cheng, J.-X.; Yan, H.; Liu, Y. High-Quality Manganese-Doped Zinc Sulfide Quantum Rods with Tunable Dual-Color and Multiphoton Emissions. *J. Am. Chem. Soc.* **2011**, *133*, 5389–5396.

8. Koh, W.-k.; Bartnik, A. C.; Wise, F. W.; Murray, C. B. Synthesis of Monodisperse PbSe Nanorods: A Case for Oriented Attachment. *J. Am. Chem. Soc.* **2010**, *132*, 3909–3913.

9. Avouris, P. Graphene: Electronic and Photonic Properties and Devices. *Nano Lett.* **2010**, *10*, 4285–4294.

10. Inagaki, M.; Kim, Y. A.; Endo, M. Graphene: Preparation and Structural Perfection. *J. Mater. Chem.* **2011**, *21*, 3280–3294.

11. Yoo, E.; Kim, J.; Hosono, E.; Zhou, H.; Kudo, T.; Honma, I. Large Reversible Li Storage of Graphene Nanosheet Families for Use in Rechargeable Lithium Ion Batteries. *Nano Lett.* **2008**, *8*, 2277–2282.

12. Novoselov, K. S.; Geim, A. K.; Morozov, S. V.; Jiang, D.; Katsnelson, M. I.; Grigorieva, I. V.; Dubonos, S. V.; Firsov, A. A. Two-Dimensional Gas of Massless Dirac Fermions in Graphene. *Nature* **2005**, *438*, 197–200.

13. Reddy, A. L. M.; Srivastava, A.; Gowda, S. R.; Gullapalli, H.; Dubey, M.; Ajayan, P. M. Synthesis of Nitrogen-Doped Graphene Films for Lithium Battery Application. *ACS Nano* **2010**, *4*, 6337–6342.

14. Zhu, J.; Yin, Z.; Li, H.; Tan, H.; Chow, C. L.; Zhang, H.; Hng, H. H.; Ma, J.; Yan, Q. Bottom-Up Preparation of Porous Metal-Oxide Ultrathin Sheets with Adjustable Composition/Phases and Their Applications. *Small* **2011**, *7*, 3458–3464.

15. Jang, J.; Jeong, S.; Seo, J.; Kim, M.; Sim, E.; Oh, Y.; Nam, S.; Park, B.; Cheon, J. Ultrathin Zirconium Disulfide Nanodiscs. *J. Am. Chem. Soc.* **2011**, *133*, 7636–7639.

16. Chang, K.; Chen, W. L-Cysteine-Assisted Synthesis of Layered MoS_2/Graphene Composites with Excellent Electrochemical Performances for Lithium Ion Batteries. *ACS Nano* **2011**, *5*, 4720–4728.

17. Ramakrishna Matte, H. S. S.; Gomathi, A.; Manna, A. K.; Late, D. J.; Datta, R.; Pati, S. K.; Rao, C. N. R. MoS_2 and WS_2 Analogues of Graphene. *Angew. Chem., Int. Ed.* **2010**, *49*, 4059–4062.

18. Schliehe, C.; Juarez, B. H.; Pelletier, M.; Jander, S.; Greshnykh, D.; Nagel, M.; Meyer, A.; Foerster, S.; Kornowski, A.; *et al*. Ultrathin PbS Sheets by Two-Dimensional Oriented Attachment. *Science* **2010**, *329*, 550–553.

19. Tang, Z.; Zhang, Z.; Wang, Y.; Glotzer, S. C.; Kotov, N. A. Self-Assembly of CdTe Nanocrystals into Free-Floating Sheets. *Science* **2006**, *314*, 274–278.

20. Vaughn, D. D.; In, S.-I.; Schaak, R. E. A Precursor-Limited Nanoparticle Coalescence Pathway for Tuning the Thickness of Laterally-Uniform Colloidal Nanosheets: The Case of SnSe. *ACS Nano* **2011**, *5*, 8852–8860.

21. Whittingham, M. S. Lithium Batteries and Cathode Materials. *Chem. Rev.* **2004**, *104*, 4271–4302.

22. Wu, B.; Song, H.; Zhou, J.; Chen, X., Iron Sulfide-Embedded Carbon Microsphere Anode Material with High-Rate Performance for Lithium-Ion Batteries. *Chem. Commun.* 47, 8653-8655.

23. Chung, J. S.; Sohn, H. J. Electrochemical Behaviors of CuS as a Cathode Material for Lithium Secondary Batteries. *J. Power Sources* **2002**, *108*, 226–231.

24. Kim, Y.; Goodenough, J. B. Lithium Insertion into Transition-Metal Monosulfides: Tuning the Position of the Metal 4s Band. *J. Phys. Chem.C* **2008**, *112*, 15060–15064.

25. Ji, X. L.; Lee, K. T.; Nazar, L. F. A Highly Ordered Nanostructured Carbon–Sulphur Cathode for Lithium–Sulphur Batteries. *Nat. Mater.* **2009**, *8*, 500–506.

26. Yang, Y.; Yu, G.; Cha, J. J.; Wu, H.; Vosgueritchian, M.; Yao, Y.; Bao, Z.; Cui, Y. Improving the Performance of Lithium–Sulfur Batteries by Conductive Polymer Coating. *ACS Nano* **2011**, *5*, 9187–9193.

27. Ji, X.; Lee, K. T.; Nazar, L. F. A Highly Ordered Nanostructured Carbon–Sulphur Cathode for Lithium–Sulphur Batteries. *Nat. Mater.* **2009**, *8*, 500–506.

28. Seo, J.; Jun, Y.; Park, S.; Nah, H.; Moon, T.; Park, B.; Kim, J.; Kim, Y.; Cheon, J. Two-Dimensional Nanosheet Crystals. *Angew. Chem., Int. Ed.* **2007**, *46*, 8828–8831.

29. Choi, J.; Jin, J.; Jung, I. G.; Kim, J. M.; Kim, H. J.; Son, S. U. $SnSe_2$ Nanoplate–Graphene Composites as Anode Materials for Lithium Ion Batteries. *Chem. Commun.* **2011**, *47*, 5241–5243.

30. Kim, B.-C.; Takada, K.; Ohta, N.; Seino, Y.; Zhang, L.; Wada, H.; Sasaki, T. All Solid State Li-Ion Secondary Battery with FeS Anode. *Solid State Ionics* **2005**, *176*, 2383–2387.

31. Cheng, F.; Huang, K.; Liu, S.; Liu, J.; Deng, R. Surfactant Carbonization to Synthesize Pseudocubic α-Fe_2O_3/C Nanocomposite and Its Electrochemical Performance in Lithium-Ion Batteries. *Electrochim. Acta* **2011**, *56*, 5593–5598.

32. Hassan, M. F.; Rahman, M. M.; Guo, Z. P.; Chen, Z. X.; Liu, H. K. Solvent-Assisted Molten Salt Process: A New Route to Synthesise α-Fe_2O_3/C Nanocomposite and Its Electrochemical Performance in Lithium-Ion Batteries. *Electrochim. Acta* **2010**, *55*, 5006–5013.

33. Tian, L.; Yep, L. Y.; Ong, T. T.; Yi, J.; Ding, J.; Vittal, J. J. Synthesis of NiS and MnS Nanocrystals from the Molecular Precursors (TMEDA)M(SC{O}$C_6H_5)_2$ (M = Ni, Mn). *Cryst. Growth Des.* **2008**, *9*, 352–357.

34. Xu, Z.; Shen, C.; Hou, Y.; Gao, H.; Sun, S. Oleylamine as Both Reducing Agent and Stabilizer in a Facile Synthesis of Magnetite Nanoparticles. *Chem. Mater.* **2009**, *21*, 1778–1780.

35. Tang, Z.; Kotov, N. A. One-Dimensional Assemblies of Nanoparticles: Preparation, Properties, and Promise. *Adv. Mater.* **2005**, *17*, 951–962.

36. Wang, W. Z.; Poudel, B.; Yang, J.; Wang, D. Z.; Ren, Z. F. High-yield Synthesis of Single-Crystalline Antimony Telluride Hexagonal Nanoplates Using a Solvothermal Approach. *J. Am. Chem. Soc.* **2005**, *127*, 13792–13793.

37. Saadat, S.; Tay, Y. Y.; Zhu, J. X.; Teh, P. F.; Maleksaeedi, S.; Shahjamali, M. M.; Shakerzadeh, M.; Srinivasan, M.; Tay, B. Y.; *et al*. Template-free Electrochemical Deposition of Interconnected ZnSb Nanoflakes for Li-Ion Battery Anodes. *Chem. Mater.* **2011**, *23*, 1032–1038.

38. Kühnle, A.; Vollmer, S.; Linderoth, T. R.; Witte, G.; Besenbacher, F. Adsorption of Dodecanethiol on Cu(110): Structural Ordering upon Thiolate Formation. *Langmuir* **2002**, *18*, 5558–5565.

39. O'Dwyer, C.; Lavayen, V.; Fuenzalida, D.; Lozano, H.; Ana, M. A. S.; Benavente, E.; González, G.; Sotomayor Torres, C. M. Low-Dimensional, Hinged Bar-Code Metal Oxide Layers and Free-Standing, Ordered Organic Nanostructures from Turbostratic Vanadium Oxide. *Small* **2008**, *4*, 990–1000.

40. Raman, N. K.; Anderson, M. T.; Brinker, C. J. Template-Based Approaches to the Preparation of Amorphous, Nanoporous Silicas. *Chem. Mater.* **1996**, *8*, 1682–1701.

41. Xu, D.; Liu, Z.; Liang, J.; Qian, Y. Solvothermal Synthesis of CdS Nanowires in a Mixed Solvent of Ethylenediamine and Dodecanethiol. *J. Phys. Chem.B* **2005**, *109*, 14344–14349.

42. Choi, S.; An, K.; Kim, E.; Yu, J. H.; Kim, J. H.; Hyeon, T. Simple and Generalized Synthesis of Semiconducting Metal Sulfide Nanocrystals. *Adv. Funct. Mater.* **2009**, *19*, 1645–1649.

43. Li, N.; Zhang, X.; Chen, S.; Yang, W.; Kang, H.; Tan, W. One-Pot Self-Assembly of Flower-like Cu_2S Structures with Near-Infrared Photoluminescent Properties. *CrystEngComm* **2011**, *13*, 6549.

44. Zhuang, Z.; Lu, X.; Peng, Q.; Li, Y. A Facile "Dispersion–Decomposition" Route to Metal Sulfide Nanocrystals. *Chem.—Eur. J.* **2011**, *17*, 10445–10452.

45. Kuzuya, T.; Tai, Y.; Yamamuro, S.; Sumiyama, K. Synthesis of Copper and Zinc Sulfide Nanocrystals *via* Thermolysis of the PolymetallicThiolate Cage. *Sci. Technol. Adv. Mater.* **2005**, *6*, 84–90.

46. Saadat, S.; Zhu, J.; Shahjamali, M. M.; Maleksaeedi, S.; Tay, Y. Y.; Tay, B. Y.; Hng, H. H.; Ma, J.; Yan, Q. Template Free Electrochemical Deposition of ZnSb Nanotubes for Li Ion Battery Anodes. *Chem. Commun.* **2011**, *47*, 9849–9851.

47. Golodnitsky, D.; Peled, E. Pyrite as Cathode Insertion Material in Rechargeable Lithium/Composite Polymer Electrolyte Batteries. *Electrochim. Acta* **1999**, *45*, 335–350.

48. Zhu, J. X.; Zhu, T.; Zhou, X. Z.; Zhang, Y. Y.; Lou, X. W.; Chen, X. D.; Zhang, H.; Hng, H. H.; Yan, Q. Y. Facile Synthesis of

Metal Oxide/Reduced Graphene Oxide Hybrids with High Lithium Storage Capacity and Stable Cyclability. *Nanoscale* **2011**, *3*, 1084–1089.

49. Chen, J. S.; Tan, Y. L.; Li, C. M.; Cheah, Y. L.; Luan, D.; Madhavi, S.; Boey, F. Y. C.; Archer, L. A.; Lou, X. W. Constructing Hierarchical Spheres from Large Ultrathin Anatase TiO_2 Nanosheets with Nearly 100% Exposed (001) Facets for Fast Reversible Lithium Storage. *J. Am. Chem. Soc.* **2010**, *132*, 6124–6130.

50. Reddy, M. V.; Yu, T.; Sow, C. H.; Shen, Z. X.; Lim, C. T.; Subba Rao, G. V.; Chowdari, B. V. R. α-Fe_2O_3 Nanoflakes as an Anode Material for Li-Ion Batteries. *Adv. Funct. Mater.* **2007**, *17*, 2792–2799.

51. Chen, J.; Xu, L.; Li, W.; Gou, X. α-Fe_2O_3 Nanotubes in Gas Sensor and Lithium-Ion Battery Applications. *Adv. Mater.* **2005**, *17*, 582–586.

52. Cui, Z.-M.; Jiang, L.-Y.; Song, W.-G.; Guo, Y.-G. High-Yield Gas−Liquid Interfacial Synthesis of Highly Dispersed Fe_3O_4 Nanocrystals and Their Application in Lithium-Ion Batteries. *Chem. Mater.* **2009**, *21*, 1162–1166.

53. Zhu, J.; Lu, Z.; Oo, M. O.; Hng, H. H.; Ma, J.; Zhang, H.; Yan, Q. Synergetic Approach to Achieve Enhanced Lithium Ion Storage Performance in Ternary Phased SnO_2−Fe_2O_3/rGO Composite Nanostructures. *J. Mater. Chem.* **2011**, *21*, 12770.